





# Assessing the Robustness of LiDAR, Radar and Depth Cameras Against Ill-Reflecting Surfaces in Autonomous Vehicles: An Experimental Study

**Conference Paper****Author(s):**

Lötscher, Michael; Baumann, Nicolas ; Ghignone, Edoardo ; Ronco, Andrea ; Magno, Michele 

**Publication date:**

2023

**Permanent link:**

<https://doi.org/10.3929/ethz-b-000641560>

**Rights / license:**

[In Copyright - Non-Commercial Use Permitted](#)

# Assessing the Robustness of LiDAR, Radar and Depth Cameras Against Ill-Reflecting Surfaces in Autonomous Vehicles: An Experimental Study

Michael Lötscher, Nicolas Baumann, Edoardo Ghignone, Andrea Ronco, Michele Magno  
Department of Information Technology and Electrical Engineering, ETH Zurich  
Zürich, Switzerland

mloetscher@ethz.ch, {nicolas.baumann, edoardo.ghignone, andrea.ronco, michele.magno}@pbl.ee.ethz.ch

**Abstract**—Range-measuring sensors play a critical role in autonomous driving systems. While Light Detection and Ranging (LiDAR) technology has been dominant, its vulnerability to adverse weather conditions is well-documented. This paper focuses on secondary adverse conditions – the implications of ill-reflective surfaces on range measurement sensors. We assess the influence of this condition on the three primary ranging modalities used in autonomous mobile robotics: LiDAR, Radio Detection and Ranging (RADAR), and Depth-Camera. Based on accurate experimental evaluation the paper’s findings reveal that under ill-reflectivity, LiDAR ranging performance drops significantly to 33% of its nominal operating conditions, whereas RADAR and Depth-Cameras maintain up to 100% of their nominal distance ranging capabilities. Additionally, we demonstrate on a 1:10 scaled autonomous racecar how ill-reflectivity adversely impacts downstream robotics tasks, highlighting the necessity for robust range sensing in autonomous driving.

**Index Terms**—Ranging Sensors, Time-of-Flight, LiDAR, RADAR, Depth-Camera, Autonomous Driving

## I. INTRODUCTION

In the context of today’s Internet of Things (IoT)-driven world, where autonomous agents are becoming increasingly integrated into various aspects of daily life, from self-driving cars [1] to robotic platforms for retirement communities [2], and collaborative drones in smart cities [3], evaluating the robustness of these autonomous robot systems is paramount. As such, precise and robust range measurements play a critical role in ensuring the correct operation of the majority of autonomous mobile robotic systems, serving as a fundamental element in many mapping and localization algorithms [4, 5].

This principle is particularly significant in the realm of autonomous driving, where mapping and localization function as vital elements in the core robotics tasks of planning [6, 7] and subsequent control strategies [7, 8], directly influencing the safety of roads. As highlighted for the case of RADAR sensors in [9], ensuring the accuracy and reliability of these measurements is critical for the effective functioning of autonomous vehicles, contributing to enhanced road safety and overall public well-being. Consequently, the importance of range measurements cannot be overstated, as they constitute one of the primary exteroceptive modalities in the considered systems [4, 10].

Among the variety of sensors utilized in autonomous driving, LiDAR is a dominant player due to its high range and accuracy

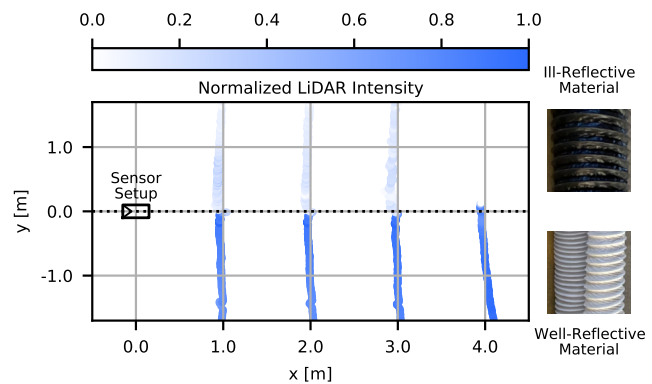


Figure 1. A visualization of how ill-reflective surfaces perturb the LiDAR range measurements at different distances. The plot has been rescaled in order to align the sensor setup (on the left) with the axes. On the top half the range measurements are taken on ill-reflective material, and on the bottom one on well-reflective material. A sample of the corresponding surface is also shown on the right.

in distance measurements [10]. This is reflected by LiDAR’s prevalent use in many autonomous driving Machine Learning (ML) datasets: when considering the survey by Feng et al. [10], 86% of the datasets (18 out of 21) contain LiDAR data.

However, despite its wide adoption, recent studies reveal that LiDAR sensors, although superior under nominal conditions, are susceptible to adverse conditions [11, 12, 13, 14]. This susceptibility implies that LiDAR sensor readings are not entirely reliable under adverse conditions, which can, in turn, affect downstream robotic tasks in autonomous driving due to inaccurate range measurements. Therefore, it is crucial to road safety and the wider acceptance of autonomous driving, to ensure robust and reliable range sensor readings [4].

In contrast to previous robustness evaluations of autonomous driving sensor modalities, that primarily concentrate on adverse weather conditions [11] or explicitly adversarial attackers [15], this work focuses on a second fundamental and pivotal concern: the challenge of ill-reflecting surfaces. As discussed later in Section II, the principle of active exteroceptive Time of Flight (ToF) sensors such as LiDAR and RADAR is fundamentally linked to the reflectivity properties of the objects being measured. For instance, diffuse and dark-colored objects reflect

significantly less signal, thus proving more challenging for range measurement sensors to detect, as demonstrated in Fig. 1, where it can be seen that the diffuse and black-colored tubes are factually invisible to the LiDAR starting already at a close range. Therefore, ill-reflecting objects, such as a dark-painted car with a matt paint finish, pose a common and great challenge to autonomous driving.

Hence, this study investigates the robustness with respect to ill-reflecting surfaces of the three most widely used range measurement sensors in mobile robotics: *LiDAR*, *RADAR* and *Depth-Camera*. Furthermore, we explore their impact on downstream robotics tasks, particularly the localization of an autonomous racing car. Our study utilizes a 1:10 scaled autonomous racing platform known as F1TENTH [16, 17]. This platform facilitates safe, cost-effective, and rapid prototyping and has been instrumental in illustrating the principles and fundamentals of autonomous driving in various robotic tasks such as perception [5, 18], planning [19] and control [20, 21].

## II. BACKGROUND

In the realm of autonomous navigation, range sensors are instrumental in providing an understanding of the environment by creating a point cloud representation. This offers the necessary data required for tasks such as object detection, mapping, and localization. The following section presents the operating principles of the employed sensors in this study.

### A. LiDAR

LiDAR is a ToF sensor utilizing laser light in the Near-Infrared Radiation (NIR) regime, hence a range estimate is produced based on the time needed for the light to reach the measurement target and return. It is comprised of a transmitter, which directs a collimated beam onto an object. This beam's trajectory is usually manipulated by a mechanical mechanism, utilizing a rotating mirror to sweep the beam across a specific scene for comprehensive coverage. A receiver then detects the portion of the reflected light, that aligns closely with the path of emitted beam [22].

This study examined the *Hokuyo UST-10LX*, which scans the environment in a 2D plane with a sampling rate of 40 Hz and a range of 10 m [23], thus making it ideal for applications in scaled mobile robotics and autonomous driving.

### B. Frequency Modulated Continuous Wave (FMCW) RADAR

RADARs sense the surroundings by illuminating the target with an electromagnetic signal and measuring the properties of the reflected (echo) signal. Different RADAR categories are defined based on the illumination signal's properties.

FMCW RADARs utilize frequency modulation to resolve the position and the relative velocity of the targets simultaneously, which makes them a favorite choice in robotics and automotive applications. They operate on the baseband signal, also called *Beat* or Intermediate Frequency (IF) signal, which is obtained by mixing the transmitted signal with the received echo. Important characteristics of FMCW radar systems are the carrier

frequency  $f_c$ , the chirp bandwidth  $B$ , and the sampling rate of the IF signal  $f_s$ .

The distance of the target can be resolved in the frequency domain, as it is directly proportional to the frequency of the beat signal, with a distance resolution of  $\frac{c}{2B}$  where  $c$  is the speed of light. Once the object is resolved in distance, its velocity can be estimated by measuring the phase difference of two consecutive chirps at the corresponding range. The speed resolution is  $\frac{\lambda}{4T_s}$ , where  $\lambda$  is the wavelength of the carrier frequency, and  $T_s$  is the time resolution on the IF signal. In practice, more than two chirps are necessary to separate different targets at the same range properly. When multiple antennas are available, it is also possible to estimate the Angle of Arrival (AoA) of the signal through the process of digital beamforming. This step, combined with a Constant False Alarm Rate (CFAR) filter, is essential for generating RADAR point clouds.

In this paper we evaluated the *Texas Instruments IWR1443*, which operates in the frequency range 76 GHz-81 GHz and offers a ranging rate of 30 Hz, with a maximum TX power of 12 dBm.

### C. Depth-Camera

In the context of this paper, a Depth-Camera, specifically an *Intel Realsense D455*, serves as an effective tool for the 3D reconstruction of the scene by creating a point cloud from the calculated distances. The camera achieves range measurements up to a distance of 6 m with a framerate of up to 90 Hz, at a resolution of  $1280 \times 720$  pixel with a global shutter sensor [24].

The operational mechanics of this Depth-Camera incorporate an Infrared Radiation (IR) stereo module. Its camera projects infrared light onto the scene, illuminating it and capturing the reflected portion. Two cameras, situated at a known distance apart from each other, a measure, referred to as the baseline  $b$ , capture the scene from slightly different perspectives, similar to how human vision functions.

In this stereo vision setup, the disparity  $d$  plays a vital role. Disparity refers to the difference in the apparent position of an object seen from the two cameras' perspectives. It is directly proportional to the distance between the object and the camera setup. Thus, by calculating the disparity, the depth  $z$  of each point in the scene can be derived, as shown in Eq. (1).

$$z = \frac{bf}{d} \quad (1)$$

The focal length  $f$ , is an intrinsic camera parameter and can be obtained by employing camera calibration techniques [25], which assess the capability of the camera lens to focus light.

## III. EXPERIMENTAL SETUP

This section provides comprehensive information on the experimental setup designed to assess the robustness of different sensor modalities' range measurements. The evaluation is organized into three primary components: reflectivity characteristics measurements of the boundary materials, static range measurements to determine the data quality under varying

reflectivity conditions, and dynamic range measurements to analyze the impact of range measurement quality on subsequent robotic tasks.

### A. Material Evaluation

The materials selected for this analysis were exhaust tubes made from Polyvinyl Chloride (PVC), chosen for their unique color, surface texture, and reflectivity attributes. The materials include a well-reflecting, white-colored, matt material serving as a baseline, and a black-colored, diffuse material with low reflectivity to examine sensor performance under challenging conditions. The material in question can be seen in Fig. 1.

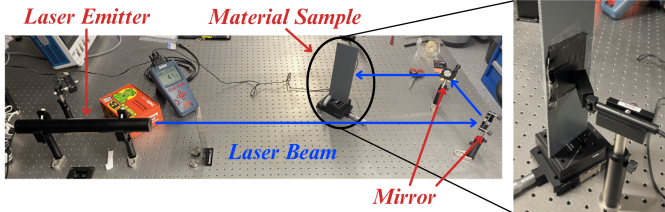


Figure 2. Setup to determine the power reflectivity  $R$  by measuring the reflected power of the target material. The emitted laser beam is directed onto the sample via two mirrors and reflected subsequently at the target sample, whereupon the reflected component is measured by the detector.

To characterize the power reflectivity  $R$  of these materials, an experiment was set up, as in Fig. 2, using a helium-neon laser, which emits continuous waves with a power of 5 mW at a wavelength of 632.8 nm. An *OPHIR PD300 UV* wide spectral range photodiode detector was used to measure the intensity of the reflected beams. The power reflectivity of the materials was recorded at twelve different locations on the sample, for both s- and p-polarization states.

### B. Static Experiment

For the static range measurements, a setup, similar to the one described by Cooper et al. [26], was used. The sensor was positioned at a fixed distance from the tube, with data collection taking place for a consistent duration of 10 s for each measurement. The gathered data points were then compared to the *ground truth* determined through a *Bosch PLR 40C* rangefinder and a rolling meter, to gauge the sensor’s accuracy. An exemplary depiction of the static reflectivity setup can be seen in Fig. 3.

### C. Dynamic Experiment

The dynamic range measurement experiment was conducted on an oval-shaped racetrack, designed to simulate a mix of ideal and adverse conditions, half of the track featured well-reflective boundaries while the other half had ill-reflective ones. Ten consecutive laps were driven to gather data for each sensor’s output, which was then processed by the localization, planning, and control systems of the robotic stack. The average lap time was computed to evaluate the overall performance.

A data-level sensor fusion approach was implemented to combine the data from the LiDAR, RADAR, and Depth-Camera sensors. The data from LiDAR was given priority due to its

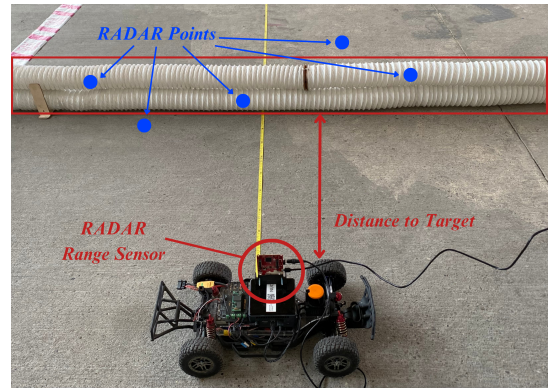


Figure 3. Experimental setup for the static performance assessment of the sensors, with the RADAR sensor as an example. Blue RADAR points are illustrated as a qualitative visualization of range measurements.

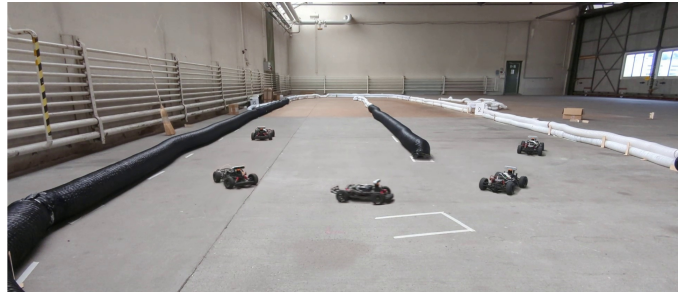


Figure 4. Oval-shaped racetrack setup designed for evaluating the lap times of various sensor configurations. The track is characterized by its distinct half-and-half boundary, composed of a black, ill-reflectivity sector and a white, well-reflecting one.

superior performance in static experiments, while the Depth-Camera and RADAR data were utilized when LiDAR data was unavailable. The aim of this dynamic experiment was to understand how sensor configurations and range measurement quality can impact the racecar’s behavior under varying environmental conditions.

## IV. PERFORMANCE EVALUATION PARAMETERS

The Mean Absolute Error (MAE) and standard deviation performance parameters are employed in this paper. They quantify the accuracy and variability of the sensor measurements. The MAE provides a measure of the average magnitude of error in a set of predictions, without considering their direction. It is calculated as the average over the verification sample of the absolute values of the differences between the forecast and the corresponding observation, as shown in Eq. (2).

$$\text{MAE} = \frac{1}{N} \sum_{i=1}^N |y_i - \hat{y}_i| \quad (2)$$

In the equation shown,  $y_i$  denotes the ground truth range, while  $\hat{y}_i$  denotes the range measured by the sensors.  $N$  is the total number of samples. The standard deviation, on the other hand, measures the dispersion of the measured data. It is used to quantify the amount of variation in a set of values. A low standard deviation indicates that the values tend to be close to



the mean of the data, while a high standard deviation indicates that the values are spread out over a wider range. The formula of the standard deviation is described in Eq. (3).

$$\sigma = \sqrt{\frac{1}{N} \sum_{i=1}^N (y_i - \bar{y})^2} \quad (3)$$

The mean of all sensor readings is denoted by  $\bar{y}$ , while each individual sensor reading is indicated by  $y_i$ .  $N$  stands for the total number of samples. A lower value for the standard deviation  $\sigma$  is more desirable, as it suggests a lower variation across the measurements.

## V. RESULTS

The results of the experiments described in Section III are presented and discussed in this section.

### A. Boundary Reflectivity Measurements

The experimental data detailed in Table I highlights the contrasting reflectivity characteristics of the black and white colored materials under varying polarization conditions and their implications on range sensor performance. The power reflectivity  $R$  is the divisor of the incident and reflected power, as seen in Eq. (4). The incident beam power  $P_i$  was measured as 4.63 mW.

$$R = \frac{P_r}{P_i} \quad (4)$$

The standard deviation of  $R$  is calculated using Gaussian error propagation under the assumption, that the standard deviation of the incident beam power  $\sigma_{P_i}$  can be neglected and therefore simplifies to Eq. (5).

$$\sigma_R = \frac{\sigma_{P_r}}{P_i} \quad (5)$$

The reflected power  $P_r$  and the power reflectivity  $R$  of the white-colored material surpass those of the black-colored material for both p-polarized and s-polarized incident light. For the white-colored material, the maximum observed power reflectivity reached 9.5%, in stark contrast with the much lower 4.7% and 0.3% recorded for the black-colored material under s- and p-polarized light respectively. Although higher than the power reflectivities seen for the black-colored material, the white material is still within a relatively low reflectivity range. Interestingly, the power reflectivity of the black-colored material is 13 times lower when exposed to a p-polarized incident laser compared to an s-polarized laser, marking a significant difference.

The distinct reflectivity characteristics of the white-colored and black-colored materials express a clear comparative advantage for the white material. These properties serve as an optimal test bed for assessing sensor performance across a range of conditions. The relatively higher reflectivity of the white-colored material provides a baseline for standard environments, while the ill-reflectivity of the black-colored material allows for the examination of sensor performance

under more challenging, adverse conditions. This range of reflectivities facilitates investigations into optimizing sensor configurations to tune effectively across diverse settings.

TABLE I. Reflectivity properties of ill-reflective black-colored boundaries and well-reflective white-colored boundaries. Mean reflected power  $P_r$  in  $\mu W$ ; Standard deviation  $\sigma_{P_r}$  in  $\mu W$ ; Power reflectivity  $R$  (dimensionless); Standard deviation  $\sigma_R$  (dimensionless).

	Black mat.		White mat.	
	p-pol.	s-pol.	s-pol.	p-pol.
$P_r$ [ $\mu W$ ]	14.08	219.63	367.42	<b>440.75</b>
$\sigma_{P_r}$ [ $\mu W$ ]	<b>1.70</b>	25.54	54.79	76.70
$R$ [ $\cdot 10^{-3}$ ]	3.041	47.436	79.356	<b>95.194</b>
$\sigma_R$ [ $\cdot 10^{-3}$ ]	<b>0.367</b>	5.516	11.834	16.566

### B. Static Range Measurements

The outcomes of the static experiment conducted on the well-reflective baseline material, are illustrated in Fig. 5. The LiDAR sensor exhibits the most extensive range for this material, reaching its maximum range of 10 m, achieving the manufacturer's specified maximum range [23]. This surpasses the RADAR sensor's maximum range of 7 m and the Depth-Camera's limit of 6 m. The LiDAR's range measurements maintain a MAE that is bound below 5 cm up to a distance of 8.5 m, however growing drastically beyond this mark.

The RADAR sensor's performance is comparable to the LiDAR's performance. However, it achieves only a maximum range of 7 m and shows a mostly constant but larger MAE between 10 to 15 cm.

Contrary to the consistent accuracy of the LiDAR and RADAR sensor, the accuracy of the Depth-Camera's measurements is monotonically decreasing as the distance from the target increases. This trend is witnessed in both the MAE as well as the standard deviation. Consequently, the MAE is resulting in 61 cm at a distance of 6 m to the Depth-Camera.

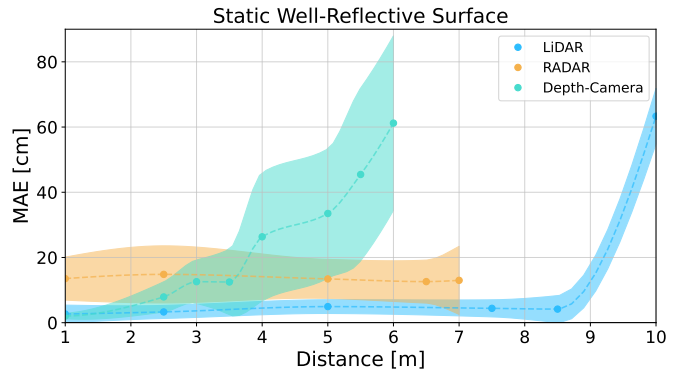


Figure 5. Comparison of LiDAR, RADAR and Depth-Camera sensor in terms of range and MAE, when sensing *well-reflective* boundaries. The standard deviation of the measurements is represented by the shaded regions. Lower is better.

In Fig. 6, the static experiment results for the ill-reflecting surface are shown. The LiDAR sensor’s behavior is similar as for the other material shown in Fig. 5, maintaining a low and mostly consistent MAE and standard deviation throughout. However, its maximum range is significantly lower, achieving at most a range of 3 m. Therefore, we see that now the maximum ranging distance has been reduced to 33% of the baseline sensing capabilities.

The Depth-Camera sensor replicates its performance pattern observed with the baseline material, exhibiting the same maximum range and upward MAE trend. However, the actual error of the MAE is significantly lower at distances from the target to the sensor higher than 3 m.

An almost constant MAE, as well as standard deviation, is achieved by the RADAR when measuring from a distance of 2.5 m onwards. The sensor manages to keep the MAE remaining below an error of 10 cm for this range. Notably, the maximum range of the RADAR is 7.5 m, the highest of all sensors for the ill-reflective surface. Despite these strengths, an observable anomaly occurs at shorter distances, where false positives appear more frequently, causing both MAE and standard deviation to surge compared to their values at larger distances. Overall, the RADAR outperforms the LiDAR and Depth-Camera counterparts in range and accuracy for distances larger than 2.5 m for the ill-reflective material.

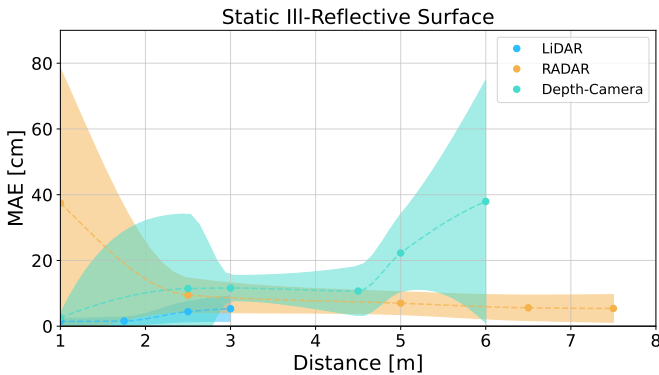


Figure 6. Comparison of LiDAR, RADAR and Depth-Camera sensor in terms of range and MAE, when sensing an *ill-reflecting* surface. The standard deviation of the measurements is represented by the shaded regions. Lower is better.

### C. Dynamic Range Measurements

Fig. 7 presents the mean lap times for each of the sensor combinations. The LiDAR + Depth-Camera configuration achieves the fastest lap times with a mean lap time of 7.686 s. It outperforms both the LiDAR-only configuration as well as the LiDAR + RADAR fusion. Specifically, the LiDAR-only configuration achieves a lap time of 7.729 s and lags by 0.043 s, hence a 0.573% deterioration, while the LiDAR + RADAR fusion’s lap times are considerably slower with 8.011 s, hence 12.026% relative to the LiDAR + Depth-Camera setup. Notably, the lap times variance is well contained across all configurations, showing a maximum standard deviation of no more than 0.054 s

for all three configurations. This deviation accounts for 0.068 s in the context of the LiDAR + Depth-Camera fusion, attesting to the consistency of the performance across the trials.

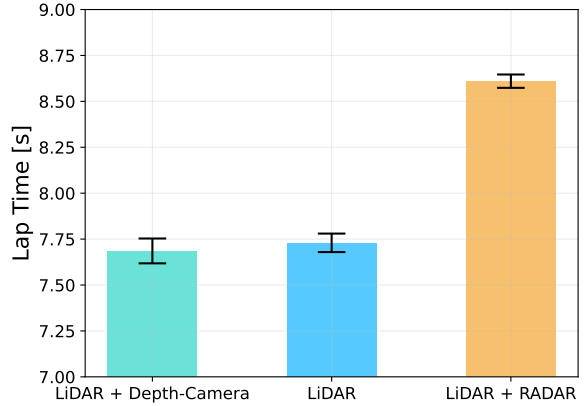


Figure 7. Comparison of the mean lap times achieved by the LiDAR-only with 7.729 s, LiDAR + Depth-Camera Fusion with 7.686 s and LiDAR + RADAR with 8.011 s, sensor fusion configurations. Lower is better.

## VI. CONCLUSION

This paper highlights the substantial influence of ill-reflective materials on the ranging capabilities of exteroceptive sensors, such as LiDAR, RADAR, and Depth-Cameras. By shedding light on the effects of ill-reflectivity on autonomous mobile robotic systems, particularly within the realm of autonomous driving, our study underscores the importance of robust and precise range sensing in enhancing road safety. As we embrace the advancements of IoT in shaping autonomous technologies, our research contributes to the broader goal of making roads safer and more reliable for all users. Hence, an assessment of static ranging abilities linked to these sensor modalities exposes that, although LiDAR yields the highest and most consistent ranging capabilities under nominal conditions, these degrade to a mere 33% under the adverse condition of ill-reflectivity. Conversely, other technologies such as RADAR and Depth-Cameras significantly outperform LiDAR in such scenarios, retaining full-ranging distance capabilities as under nominal conditions. Through an experimental evaluation on a 1:10 scale autonomous racing car, we demonstrate the consequential effect of the quality of ranging measurements on downstream robotics tasks. This underscores the importance of embracing multimodal ranging sensors and sensor fusion to ensure robust and reliable autonomous driving behavior.

### ACKNOWLEDGMENTS

The authors wish to express their gratitude to the Ultrafast Dynamics Group of ETH Zurich, particularly Vladimir Ovuka, for granting access to their laboratories and for supporting the conduction of our reflectivity experiments.

### REFERENCES

- [1] I. Yaqoob, L. U. Khan, S. M. A. Kazmi, M. Imran, N. Guizani, and C. S. Hong, “Autonomous driving

- cars in smart cities: Recent advances, requirements, and challenges,” *IEEE Network*, vol. 34, no. 1, pp. 174–181, 2020, doi: 10.1109/MNET.2019.1900120.
- [2] S. El-Tawab, N. Sprague, and A. Mufti, “Autonomous vehicles: Building a test-bed prototype at a controlled environment,” in *2020 IEEE 6th World Forum on Internet of Things (WF-IoT)*, 2020, pp. 1–6, doi: 10.1109/WF-IoT48130.2020.9221222.
- [3] S. H. Alsamhi, O. Ma, M. S. Ansari, and F. A. Almalki, “Survey on collaborative smart drones and internet of things for improving smartness of smart cities,” *IEEE Access*, vol. 7, pp. 128 125–128 152, 2019, doi: 10.1109/ACCESS.2019.2934998.
- [4] W. Hess, D. Kohler, H. Rapp, and D. Andor, “Real-time loop closure in 2d lidar slam,” in *2016 IEEE International Conference on Robotics and Automation (ICRA)*, 2016, pp. 1271–1278.
- [5] C. H. Walsh and S. Karaman, “Cddt: Fast approximate 2d ray casting for accelerated localization,” in *2018 IEEE International Conference on Robotics and Automation (ICRA)*, 2018, pp. 3677–3684, doi: 10.1109/ICRA.2018.8460743.
- [6] S. Karaman and E. Frazzoli, “Sampling-based algorithms for optimal motion planning,” 2011.
- [7] A. Liniger, A. Domahidi, and M. Morari, “Optimization-based autonomous racing of 1:43 scale RC cars,” *Optimal Control Applications and Methods*, vol. 36, no. 5, pp. 628–647, jul 2014, doi: 10.1002/oca.2123.
- [8] A. Liniger and J. Lygeros, “Real-time control for autonomous racing based on viability theory,” *IEEE Transactions on Control Systems Technology*, vol. 27, no. 2, pp. 464–478, mar 2019, doi: 10.1109/tcst.2017.2772903.
- [9] Y. Wang, Q. Zhang, Z. Wei, Y. Lin, and Z. Feng, “Performance analysis of coordinated interference mitigation approach for automotive radar,” *IEEE Internet of Things Journal*, vol. 10, no. 13, pp. 11 683–11 695, 2023, doi: 10.1109/JIOT.2023.3244566.
- [10] D. Feng, C. Haase-Schütz, L. Rosenbaum, H. Hertlein, C. Glaeser, F. Timm, W. Wiesbeck, and K. Dietmayer, “Deep multi-modal object detection and semantic segmentation for autonomous driving: Datasets, methods, and challenges,” *IEEE Transactions on Intelligent Transportation Systems*, 2020.
- [11] Y. Zhang, A. Carballo, H. Yang, and K. Takeda, “Perception and sensing for autonomous vehicles under adverse weather conditions: A survey,” *ISPRS Journal of Photogrammetry and Remote Sensing*, vol. 196, pp. 146–177, feb 2023, doi: 10.1016/j.isprsjprs.2022.12.021.
- [12] T. Broedermann, C. Sakaridis, D. Dai, and L. V. Gool, “Hrfuser: A multi-resolution sensor fusion architecture for 2d object detection,” 2023.
- [13] F. Nobis, M. Geisslinger, M. Weber, J. Betz, and M. Lienkamp, “A deep learning-based radar and camera sensor fusion architecture for object detection,” 2020.
- [14] S. Yao, R. Guan, X. Huang, Z. Li, X. Sha, Y. Yue, E. G. Lim, H. Seo, K. L. Man, X. Zhu, and Y. Yue, “Radar-camera fusion for object detection and semantic segmentation in autonomous driving: A comprehensive review,” 2023.
- [15] M. A. Hoque and R. Hasan, “Autonomous driving security: A comprehensive threat model of attacks and mitigation strategies,” in *2022 IEEE 8th World Forum on Internet of Things (WF-IoT)*, 2022, pp. 1–6, doi: 10.1109/WF-IoT54382.2022.10152219.
- [16] M. O’Kelly, H. Zheng, A. Jain, J. Auckley, K. Luong, and R. Mangharam, “Tunercar: A superoptimization toolchain for autonomous racing,” in *2020 IEEE International Conference on Robotics and Automation (ICRA)*, 2020, pp. 5356–5362, doi: 10.1109/ICRA40945.2020.9197080.
- [17] M. O’Kelly, H. Zheng, D. Karthik, and R. Mangharam, “F1tenth: An open-source evaluation environment for continuous control and reinforcement learning,” in *NeurIPS 2019 Competition and Demonstration Track*. PMLR, 2020, pp. 77–89.
- [18] A. Ronco, N. Baumann, M. Giordano, and M. Magno, “Towards robust velocity and position estimation of opponents for autonomous racing using low-power radar,” in *2023 9th International Workshop on Advances in Sensors and Interfaces (IWASI)*, 2023, pp. 21–26, doi: 10.1109/IWASI58316.2023.10164312.
- [19] A. Sinha, M. O’Kelly, H. Zheng, R. Mangharam, J. Duchi, and R. Tedrake, “Formulazero: Distributionally robust online adaptation via offline population synthesis,” in *Proceedings of the 37th International Conference on Machine Learning*, ser. ICML’20, 2020.
- [20] J. Becker, N. Imholz, L. Schwarzenbach, E. Ghignone, N. Baumann, and M. Magno, “Model- and acceleration-based pursuit controller for high-performance autonomous racing,” in *2023 IEEE International Conference on Robotics and Automation (ICRA)*, 2023, pp. 5276–5283, doi: 10.1109/ICRA48891.2023.10161472.
- [21] B. D. Evans, H. A. Engelbrecht, and H. W. Jordaan, “High-speed autonomous racing using trajectory-aided deep reinforcement learning,” *IEEE Robotics and Automation Letters*, vol. 8, no. 9, pp. 5353–5359, 2023, doi: 10.1109/LRA.2023.3295252.
- [22] R. Siegwart, I. R. Nourbakhsh, and D. Scaramuzza, *Introduction to Autonomous Mobile Robots*. The MIT Press, 2011, ISBN 0262015358.
- [23] Hokuyo, “Lidar ust-10lx,” [Online]. Available: <https://hokuyo-usa.com/products/lidar-obstacle-detection/ust-10lx>.
- [24] Intel, “Realsense d455,” [Online]. Available: <https://www.intelrealsense.com/depth-camera-d455/>.
- [25] L. Oth, P. Furgale, L. Kneip, and R. Siegwart, “Rolling shutter camera calibration,” in *Proceedings of the IEEE Conference on Computer Vision and Pattern Recognition (CVPR)*, June 2013.
- [26] M. A. Cooper, J. F. Raquet, and R. Patton, “Range information characterization of the hokuyo ust-20lx lidar sensor,” *Photonics*, vol. 5, no. 2, 2018.